International Journal of Thermal Sciences 48 (2009) 2187–2202

Contents lists available at ScienceDirect

International Journal of Thermal Sciences

journal homepage: www.elsevier.com/locate/ijts

A fully-coupled simulation of vortical structures in a large-scale buoyant pool fire

Sherman C.P. Cheung [a], G.H. Yeoh [b,c,*]

[a] School of Aerospace, Mechanical and Manufacturing Engineering, RMIT University, VIC 3083, Australia
[b] Australian Nuclear Science and Technology Organisation (ANSTO), PMB 1, Menai, NSW 2234, Australia
[c] School of Mechanical and Manufacturing Engineering, University of New South Wales, Sydney 2052, Australia

ARTICLE INFO

Article history:
Received 25 September 2008
Received in revised form
27 February 2009
Accepted 22 April 2009
Available online 29 May 2009

Keywords:
Buoyant pool fire
Vortical structures
Large eddy simulation
Soot radiation

ABSTRACT

A numerical study simulating the temporal vortical structures of a large-scale buoyant pool fire has been carried out using a fully-coupled Large Eddy Simulation (LES) model which incorporates all essential subgrid scale (SGS) turbulence, combustion, radiation and soot chemistry considerations. Based on the strained laminar flamelet approach, a scalar dissipation conditioned SGS combustion model is introduced to distinguish the highly non-equilibrating burn and extinguishment of flamelets commonly found in pool fires. Numerical results from the present model are validated and compared against a one-meter diameter methane pool fire experimental data and predictions from other LES field models. The predicted time-averaged velocity and temperature profiles have been found to be in good agreement with the experimental data and those numerical results. Qualitative comparisons of instantaneous velocity field against experimental data have revealed that the dynamic phenomena of large-scale vortical structures and its associated puffing behaviour of pool fire are well captured. Quantitative comparisons of velocity time history and pulsation frequency also show close agreement against experimentally evaluated quantities.

1. Introduction

The accurate prediction of the consequences of fire is crucial for the assessment of fire safety and the appropriate design for fire protection measures. Much emphasis has been given to the use of numerical methodologies in predicting the spread of smoke and transient temperature distribution as well as its associated velocity field. An in-depth understanding of pertinent flow mechanisms is still yet to be fully attained since the study of fire dynamics generally involves numerous tightly coupled phenomena associated with convective and diffusive process, buoyancy and entrainment induced fluid motion, turbulent mixing of scalar, chemical combustion process, soot formation and radiation heat transfer [1]. It is only of much recent advancement in the computational technology that the consideration of more sophisticated approaches to study the fluid and heat flow characteristics of fires can nonetheless be realised. Of particular interest in this present study is the complex behaviour of a large-scale buoyant pool fire, which shares similar chemo-physical phenomena with most other types of fires in practice.

From the period of 1970s to the 1980s, many investigators have reported the behaviour of buoyant pool fires exhibiting a periodic oscillatory motion close to their origin which has often been referred to as the "puffing" behaviour [2–5]. By inferring to their observatory studies, the pulsation of fires can be taken to be caused by the formation of large vortical structures with the corresponding length scales on the order of the fire radius. These rotational flow motions create instability to the combustion of fuel with the air entrainment and induce subsequent development of alternative "necking" and "bulging" of the flame surface. On the basis of the phenomenological reasoning and observational data of various large-scale fire experiments, Tieszen et al. [6] have further postulated three mechanisms primarily responsible for the vortical structures in fire. The three mechanisms that contribute to the three stages of vortical structure development are depicted in Fig. 1. Within the fire, static pressure gradient exists in the vertical direction as a result of the gravitational force, and the density gradient is formed by the rapid temperature change between hot gases and surrounding ambient air in the horizontal direction. The misalignment of these two gradients causes the hot and cold fluid to be twisted into rotational motions which thereby initiates the formation of vortical structures. This mechanism also known as the "baroclinic vorticity generation" which can be expressed in terms of the vector cross of the two gradients as: $(\nabla\rho \times \nabla P)/\rho^2$. As the thickness of this density layer controls the strength of the vorticity

* Corresponding author. Australian Nuclear Science and Technology Organisation (ANSTO), PMB 1, Menai, NSW 2234, Australia. Tel.: +61 2 9717 3817; fax: +61 2 9717 9263.
E-mail address: guan.yeoh@ansto.gov.au (G.H. Yeoh).

1290-0729/$ – see front matter © 2009 Elsevier Masson SAS. All rights reserved.
doi:10.1016/j.ijthermalsci.2009.04.011

Nomenclatures

a, b	Exponents of the beta probability density function
C_{I}	Constant appearing in Eq. (10)
C_p	Mixture specific heat at constant pressure
$C_{p,i}$	Specific heat of ith species at constant pressure
C_s	Turbulence SGS model coefficient
C''	Constant appearing in Eq. (16)
C_α,C_β,C_γ	Pre-exponential constants for soot quantities
D	Fire bed width
E_{b}	Blackbody radiation
f_{v}	Volume fraction
$\overline{g}$	Gravitational vector
$h^0_{\mathrm{f}i}$	Heat of formation of ith species
I_j	Radiation intensities
k	Turbulent kinetic energy
K_{a}	Gas radiative absorption coefficient
$K_{a,g}$, $K_{a,s}$	Absorption coefficients for filter gas and soot
k_A, k_B, k_T, k_Z	Reaction coefficients for soot oxidation
n	Soot particulate number density
n_j	Unit normal vector
No	Avogadro's number
p	Pressure
p'	Pressure correction
$p^{(0)}$	Zeroth-order pressure
Pr	Prandtl number
P_{o2}	Filtered partial pressure of oxygen
$\tilde{P}(f,\tilde{Z},\tilde{Z''^2})$	Beta probability density function (PDF)
$\tilde{P}(f,\chi)$	Joint PDF for mixture fraction and scalar dissipation
$\tilde{P}(f_{\mathrm{st}})$	PDF at stoichiometric condition
$\overline{q}$	Diffusion/flux vector
q_ϕ	Species diffusion flux
q_i	Heat diffusion flux
$\dot{Q}$	Total heat release rate
R	Gas constant
R_{u}	Universal gas constant
R_{ox}	Overall reaction rate
s	Stoichiometric oxygen-to-fuel mass ratio
Sc	Schmidt number
S_ϕ	Source term of scalar quantities
S_{rad}	Radiant heat energy
$S_{Z''^2}$	Mixture fraction variance source term
$S_{\zeta_{\mathrm{n}}}$	Soot particulate number density source term
$S_{\zeta_{\mathrm{s}}}$	Soot volume fraction source term
t	Time
T	Temperature
T_α, T_γ	Activation temperatures for soot quantities
u_j	Velocity components (u, v, w) along the x, y, z Cartesian coordinate
X_{fu}	Mole fraction of fuel
Y_{o}	Mass fraction of oxidant
Y_{F}, Y_{F1}	Mass fraction of fuel and fuel at the free stream
Z	Instantaneous mixture fraction

Systems

w_i	Quadrature weights associated with discrete radiation directions
W_i	Molecular weight of ith species
X	Mole fraction
Y_i	Mass fraction of ith species
Z	Mixture fraction
Z''^2	Mixture fraction variance

Greek symbols

α	Rate of particle nucleation for soot number density
β	Rate of soot coagulation
χ	Instantaneous scalar dissipation
χ_0	Local peak value of χ
δ	Rate of particle nucleation for soot volume fraction
ϵ	Dissipation rate of turbulent kinetic energy
γ	Rate of soot surface growth
λ	Thermal conductivity
μ	Molecular viscosity
$\mu_{\mathrm{T}}^{\mathrm{SGS}}$	Turbulent viscosity from SGS model
ν	Kinematic viscosity
ρ	Density
ρ_{s}	Soot density
σ	Stefan–Boltzman constant
σ_{ij}	Stress tensor
τ_i	Viscous stress tensor
ω_T	Local heat release source term
ω_i	Reaction rate of ith species
ξ_j, η_j, ζ_j	Direction cosines
ζ_n	Alternative definition of soot particulate number density
ζ_s	Alternative definition of soot volume fraction
Δ	Subgrid length scale
ΔH_{c}	Heat of combustion
ΔT	Temperature difference, $T - T_{\mathrm{ref}}$
Δx, Δy,Δz	Mesh spacings along the x, y, z Cartesian coordinate system
ϕ	Scalar quantities

Subscripts

f	Cell face
fu	Fuel
ox	Oxidant
st	Stoichiometric condition
T	Turbulent state
ref	Reference state

Superscripts

min	The minimum value
max	The maximum value
$(\bar{})$	Filtered field
$(\sim)$	Favre-Filtered field
$(^*)$	Intermediate field for the predictor step
n	Previous time level
n+1	New time level

generation, the strongest vortex formation usually occurs at the smallest scale of the flame surface (i.e. locations of the highest density gradient). These small-scale vorticities are then raised up by the presence of buoyancy forces within the fire. While they are travelling upwards, some may well combine with other eddies that are also rotating in the same sense. The occurrence of this vortices-pairing phenomenon often referred as "amalgamation" leads to the growth of larger flaming vortices and then results in the oscillatory characteristic of necking and bulging of the fire. These large-scale vortical structures undergo subsequent processes of energy

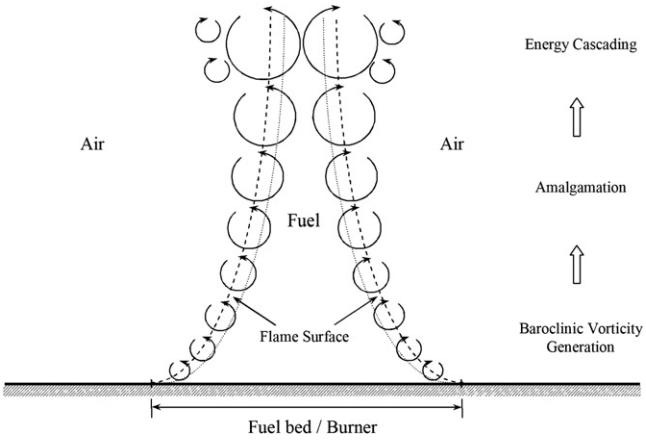

Fig. 1. A schematic of the mechanisms contribute to the three stages of vortical structure development.

cascade, which they collapse back to the smaller eddies, until they burn out at the top of the flame.

Based on the description of the aforementioned mechanisms, it must be confessed that vortical structures of fire are generated in a wide range of length scales where exothermic combustion, fluid motions and the spatial distribution of density and pressure occur in highly non-linear unsteady conditions. Modelling the periodic oscillation of pool fire (also known as pulsation frequency) is thus an extremely challenging task for fire engineers. Direct Numerical Simulation (DNS) studies have been carried out in an attempt to resolve the transient behaviour of axis-symmetric plumes [7,8]. Owing to limited computational resources, most investigations have been mainly carried out in two dimensions rather than three dimensions. Even with the present computer technology, it is still impractical to adopt DNS in resolving all the required length and time scales associated with the fire phenomena. For typical large-scale pool fires, the size of eddies can range from length scales of sub-milimeters to the order of the size of fire beds, usually in meters [6].

In order to extend the scope of investigation to practical fires, the use of turbulence models within the computational simulation is inevitable especially in the consideration of resolving the chemo-physical mechanisms down to the smallest scale of "affordable" mesh size. Macroscopic fire simulations based on time-averaged turbulence models – hereby denote as Reynolds-Averaged-Navier–Stokes (RANS) approaches – have been widely adopted in earlier studies [9–12]. Nevertheless, the RANS models have been known to be unable to capture the scale dependent dynamic behaviours which are prevalent throughout the pulsation cycle of buoyant fires. Alternatively, the Large Eddy Simulation (LES) approach, which involves direct numerical simulation of the large-scale turbulence and modelling the small-scale turbulence, has recently become the central focus of fire modelling [13–16]. Based on the spatial filtering technique, LES can provide information to match macroscopic observables (scales that are resolved on computational mesh) while the microscopic (unresolved) information are indirectly reflected by the formulation of subgrid scale (SGS) turbulence model. As the dynamic behaviours of large eddies are resolved directly, the temporal vortical structures are expected to be better captured by the LES as opposed to the RANS approach [6,17].

Baum et al. [17] have pioneered the study of buoyant plume/jet modelling using LES turbulent closure. Although the fire was modelled as a heat and smoke source, their study clearly demonstrated the potential of the application of LES in buoyant fire simulations. More comprehensive LES fire models were presented by Rawat et al. [18] and Desjardin [19] and the models have been validated against the experiment on a 1-m diameter pool fire by Tieszen et al. [20]. Rawat et al. [18] adopted the unsteady flamelet approach in order to incorporate the complex chemistry of methane into the subgrid scale combustion model. Additional models for soot and NO_x formation were also considered. A similar concept was also employed by Desjardin [19] where conditional dissipation rate model was introduced into the SGS combustion model. In both studies, predicted time-averaged velocity quantities were in good agreement with the experimental data. However, no thorough comparison were made regarding the puffing effect of the fluid and heat flow and pulsation frequency.

In-depth discussions on capturing the pulsation frequency of buoyant fire have been recently reported by Wen et al. [21]. The Fire Dynamic Simulator (FDS), developed by the National Institute of Standards and Technology, was applied to simulate a medium-scale (i.e. 0.3 m diameter) methanol pool fire. The mean values of temperature and axial velocity were successfully predicted. However, some difficulty in capturing the pulsation frequency was reported by Wen et al. [21]. In their paper, they concluded that the limitation of the computer code could have been resulted from the simplified pressure treatment within FDS. In our previous study [22,23], model predictions have been validated against the same sized pool fire fuelled by methane against the measurement by McCaffrey [24] and empirical correlations by Baum and McCaffrey [25]. Although excellent agreement of the time-averaged temperatures and velocities was achieved, the pulsation frequency from our model could not be compared except by inferring to other researchers' observations of similar pool fires. A thorough assessment of the predicted pulsation frequency from LES models remains outstanding.

Very recently, Xin et al.[26] have successfully applied the FDS model to capture the puffing frequency of a 1-m diameter pool fire measured by Tieszen et al. [20]. Quantitative validations of the predicted time-average velocities were presented and demonstrated good agreement with measurements. Their study confirmed the capability of LES models in resolving the transient vortex structure of buoyant pool fire. Nevertheless, the effect of instantaneous scalar dissipation χ was not considered in their combustion modelling. As clearly exemplified in Desjardin [19] study, the dynamic variation of scalar dissipation has a significant effect on the predicted temperatures and combustion reaction rates. Furthermore, soot particle concentrations, which also have been proven of predominant importance to radiation loss [12], were not explicitly solved within the physical sub-models. To explore the predictive nature of LES model, it is essential to develop a fully-coupled model incorporating all combustion, radiation and soot considerations within one complete simulation methodology.

The objectives of this article are two-fold: (i) further extend the SGS combustion model to include the consideration of the scalar dissipation using strained laminar flamelet approach and validate the time-averaged predictions against a large-scale (i.e. 1.0 m diameter) methane pool fire measured by Tieszen et al. [20] and (ii) present a fully-coupled model incorporating all macroscopic models and assess its capability in capturing the temporal vortical structures. This pertains directly to the pulsation frequency of which qualitative and quantitative comparisons are carried out by comparing the spatial-filtered velocity predictions with the instantaneously PIV flow field measurement of Tieszen et al. [20].

2. Mathematical formulation

The fluid motion of the pool fire is considered as a low-speed flow whereby the contribution of acoustic waves is considered to be

negligible to the flow dynamics [22]. Based on the formulation of Knio et al. [27], the low-Mach-number Favre-filtered mass, momentum, energy and scalar conservation equations in a Cartesian coordinate frame can be written as:

$$\frac{\partial \overline{\rho}}{\partial t}+\frac{\partial\left(\overline{\rho}\tilde{u}_j\right)}{\partial x_j}=0 \tag{1}$$

$$\frac{\partial\left(\overline{\rho}\tilde{u}_j\right)}{\partial t}+\frac{\partial\left(\overline{\rho}\tilde{u}_i\tilde{u}_j\right)}{\partial x_i}=-\frac{\partial \overline{p}}{\partial xj}+\frac{\partial \overline{\tau}_{ij}}{\partial x_i}-\frac{\partial \overline{\tau}_{u_iu_j}}{\partial x_i}+\left(\overline{\rho}-\rho_{\mathrm{ref}}\right)\overrightarrow{g} \tag{2}$$

$$\overline{\rho}C_p\frac{\partial \tilde{T}}{\partial t}+\overline{\rho}C_p\tilde{u}_i\frac{\partial \tilde{T}}{\partial x_i}=\frac{\partial \overline{\tau}_{u_iT}}{\partial x_i}-\frac{\partial \overline{q}_i}{\partial x_i}+\overline{\omega}_T+S_{\mathrm{rad}} \tag{3}$$

$$\frac{\partial\left(\overline{\rho}\tilde{\phi}\right)}{\partial t}+\frac{\partial\left(\overline{\rho}\tilde{u}_i\tilde{\phi}\right)}{\partial x_i}=\frac{\partial \overline{\tau}_{u_i\phi}}{\partial x_i}-\frac{\partial \overline{q}_\phi}{\partial x_i}+S_\phi \tag{4}$$

where ρ is the mixture density, u_i is the velocity vector, p is the pressure, and T is the temperature. From above, ϕ represents the scalar quantities involve in the flow system (e.g. mixture fraction, variance of mixture fraction, soot particulate density and soot volume fraction) while $\overline{\omega}_T$ depicts the filtered heat release source term. Source terms in Eqs. (3) and (4), i.e. S_{rad} and S_ϕ, describe the global radiative heat exchange and generation rate of species, respectively. They will be further discussed at a later stage.

Using Newton's, Fick's, and Fourier's laws [28], the filtered viscous stress tensor, species diffusion vector and heat flux vector in terms of resolved quantities are given by:

$$\overline{\tau}_{ij}=-\frac{2}{3}\mu\frac{\partial \tilde{u}_k}{\partial x_k}+\mu\left(\frac{\partial \tilde{u}_i}{\partial x_j}+\frac{\partial \tilde{u}_j}{\partial x_i}\right) \tag{5}$$

$$\overline{q}_i=-\frac{\mu C_p}{Pr}\frac{\partial \tilde{T}}{\partial x_i} \tag{6}$$

$$\overline{q}_\phi=-\frac{\mu}{Sc_\phi}\frac{\partial \phi}{\partial x_i} \tag{7}$$

The molecular Prandtl number Pr is set to a value of 0.7. The molecular Schmidt numbers for mixture fraction and its variance are also specified a value of 0.7 while the Schmidt numbers for soot quantities, (i.e. soot particulate number density and volume fraction) according to Sivathanu and Gore [29] are set to 700.

Based on the ideal gas law, the equation of state can be expressed as $p^{(0)}=\overline{\rho}R\tilde{T}$, where the zeroth-order pressure $p^{(0)}$ is assumed to be equivalent to the atmospheric pressure and the gas constant R is determined through $R=R_{\mathrm{u}}\sum Y_i/W_i$, where R_{u} is the universal gas constant. For the purpose of numerical implementation which will become more evident in the description of the predictor–corrector scheme, the time rate of change of density is ascertained by differentiating the equation of state,

$$\frac{\partial \overline{\rho}}{\partial t}=\overline{\rho}\left(-\frac{1}{\tilde{T}}\frac{\partial \tilde{T}}{\partial t}-\frac{1}{\sum Y_i/W_i}\sum\frac{1}{W_i}\frac{\partial \tilde{Y}_i}{\partial t}\right) \tag{8}$$

The unknown SGS correlations $\overline{\tau}_{u_iu_j}$, $\overline{\tau}_{u_iT}$, and $\overline{\tau}_{u_i\phi}$ appearing in Eqs. (2)–(4) require closure using the SGS models. Zhou et al. [30] have successfully demonstrated the feasibility of applying the Smagorinsky–Lilly model [31] to investigate unsteady low-speed buoyant jet diffusion flames. Kang and Wen [16] have also adopted the Smagorinsky–Lilly model for their study of a small-scale buoyant fire. The current SGS momentum stress is henceforth modelled according to the Smagorinsky–Lilly formulation, *viz.*,

$$\overline{\tau}_{u_iu_j}\approx 2C_s\overline{\rho}\Delta^2|\Pi_{\mathrm{G}}|\left(\tilde{S}_{ij}-\frac{1}{3}\tilde{S}_{kk}\delta_{ij}\right)-\frac{1}{3}\underbrace{2C_{\mathrm{I}}\overline{\rho}\Delta^2|\Pi_{\mathrm{G}}|^2\delta_{ij}}_{\overline{\tau}_{kk}} \tag{9}$$

where $\tilde{S}_{ij}=1/2((\partial\tilde{u}_i/\partial x_j)+(\partial\tilde{u}_j/\partial x_i))$ and $\Pi_{\mathrm{G}}=(2\tilde{S}_{ij}\tilde{S}_{ij})^{1/2}$, respectively. The subgrid length Δ is expressed as $\Delta=(\Delta x\Delta y\Delta z)^{1/3}$. Erlebacher et al. [32] suggested that $\overline{\tau}_{kk}$ may be ignored since $C_{\mathrm{I}}\ll C_s$. The Smagorinsky constant C_s is taken to be 0.2.

Similar to the resolved scale, the thermal and scalar flux vectors due to SGS motions are also correlated according to the turbulent Prandtl and Schmidt numbers. Considering the large-scale pool fire as a fully turbulent diffusion flame, the turbulent Prandtl and all scalar turbulent Schmidt numbers are prescribed values of 0.3 [33].

2.1. Subgrid scale combustion modelling

For the combustion, an infinitely fast single-step reaction is considered: F + O → tP. The main role of an SGS reaction model for turbulent non-premixed combustion is designed to incorporate the effect of subgrid fluctuations in the thermo-chemical variables on the filtered chemical source term. On the basis of the mixture fraction-based approach, all the species mass fractions can be taken to be functions of only the mixture fraction. Using this assumption, Bilger [34] derived the expression for the rate of reaction for the ith species, which can also be found in Kuo [35] in the form of

$$\omega_i=-\frac{1}{2}\rho\chi\frac{\mathrm{d}^2Y_i}{\mathrm{d}Z^2} \tag{10}$$

where χ is the instantaneous scalar dissipation given by $\chi=2D(\partial Z/\partial x_j)^2$. The instantaneous heat release rate that is required is determined for N species from

$$\omega_{\mathrm{T}}=-\sum_{i=1}^{N}h_{\mathrm{f}i}^{\mathrm{o}}\omega_i \tag{11}$$

where $h_{\mathrm{f}i}^{\mathrm{o}}$ is the ith species standard heat of formation and ω_i is given by Eq. (10).

In LES, the flame is typically not spatially resolved by the computational grid. It is therefore assumed that at the subgrid level there exists a statistical ensemble of laminar diffusion flamelets each satisfying universal state relationships. Under near-equilibrium conditions, the state relationships could be represented such as those of equilibrium chemistry assumption or experimental state relationships established by Sivathanu and Faeth [36]. In order to predict highly non-equilibrium flame events such as lift-off or extinction, the state relationships need to be modified by the consideration of the scalar dissipation and to distinguish between burning and extinguished flamelets – the strained laminar flamelet approach.

The approach based on subgrid modelling for turbulent reacting flows developed by Cook and Riley [37] for non-premixed turbulent flames is applied herein. This method accounts for finite-rate chemistry by invoking the laminar flamelet approximation and applies the Large Eddy Probability Density Function of a mixture fraction. By assuming that mixing and reaction occur in local thin regions of steady, one-dimensional, laminar counterflow flames, the instantaneous scalar dissipation χ can be determined analytically and is given by

$$\chi = \chi_o F(Z) \tag{12}$$

where the function F is the inverse of the Gaussian error function of the mixture fraction given by

$$F(Z) = \exp\left(-2\left[\mathrm{erf}^{-1}(2Z-1)\right]^2 \right) \tag{13}$$

In Eq. (12), χ_o refers to the local peak value of χ within the reaction layer. The modelling implies that χ_o is independent of Z; the filtered composition can thus be expressed as

$$\tilde{Y}_i = \int_0^1 \int_{\chi_o^{\min}}^{\chi_o^{\max}} Y_i(Z,\chi_o) P(\chi_o) P(Z)\, \mathrm{d}\chi_o \mathrm{d}Z \tag{14}$$

where $\chi_o^{\min}$ and $\chi_o^{\max}$ are the minimum and maximum values of χ_o within the LES grid cell, respectively. The $P(Z)$ and $P(\chi_o)$ are the respective subgrid scale probability density functions of Z and χ. Cook and Riley [37] demonstrate that $Y_i(Z,\chi_o)$ is a slow function of χ, and hence of χ_o [38]. Assuming that the interval $\chi_o^{\max} - \chi_o^{\min}$ is not too large, $Y_i(Z,\chi_o)$ can be approximated via the Taylor series expansion about χ_o as

$$Y_i(Z,\chi_o) \approx Y_i\left(Z,\tilde{\chi}_o\right) + \left.\frac{\partial Y_i}{\partial \chi_o}\right|_{\tilde{\chi}_o} \left(\chi_o - \tilde{\chi}_o\right) \tag{15}$$

Inserting Eq. (15) into Eq. (14) and integrating over χ_o yields

$$\tilde{Y}_i = \int_0^1 Y_i\left(Z,\tilde{\chi}_o\right) P(Z)\mathrm{d}Z \tag{16}$$

The integration in the above equation requires only the evaluation of $P(Z)$, which the approach based on a presumed shape of the probability density function is adopted for computational simplicity. For a beta function, its equivalent form is given by

$$P(Z) = \frac{Z^{\alpha-1}(1-Z)^{\beta-1}}{\int_0^1 Z^{\alpha-1}(1-Z)^{\beta-1}\mathrm{d}Z} \tag{17}$$

where a and b are two parameters of the beta function: $a = \tilde{Z}(\tilde{Z}(1-\tilde{Z})/\widetilde{Z''^2} - 1)$ and $b = (1-\tilde{Z})(\tilde{Z}(1-\tilde{Z})/\widetilde{Z''^2} - 1)$.

The filtered local peak value of χ within the layer χ_o ($\chi_o^{\min} \le \chi_o \le \chi_o^{\max}$) can be immediately obtained via Eq. (12) as

$$\tilde{\chi}_o = \frac{\tilde{\chi}}{\int_0^1 F(Z)P(Z)\mathrm{d}Z} \tag{18}$$

In the above equation, the filtered scalar dissipation $\tilde{\chi}$ is modelled according to the proposal of Jiménez et al. [39]. A simple and general model can be taken from RANS modelling of dissipation in terms of a characteristic mixing time which is assumed to be proportional to the turbulent characteristics time. In LES, the SGS scalar mixing time can be defined as

$$\frac{1}{\overline{\tau}_Z} = \frac{\tilde{\chi}}{\widetilde{Z''^2}} \tag{19}$$

An equivalent SGS turbulent characteristic time $\overline{\tau}$ can be expressed on the basis of the ratio between the SGS kinetic energy $\overline{k} = 1/2(\overline{u_i u_i} - \overline{u}_i\overline{u}_i)$ and the filtered kinetic energy dissipation rate $\overline{\varepsilon} = \overline{\nu(\partial u_i/\partial x_j \partial u_i/\partial x_j)}$. Assuming proportionality between both times, a model for $\tilde{\chi}$ can be derived as

$$\frac{\tilde{\chi}}{\widetilde{Z''^2}} = \frac{1}{\overline{\tau}_Z} \sim \frac{C}{\overline{\tau}} = C\frac{\overline{\varepsilon}}{\overline{k}} \tag{20}$$

The parameter C is assumed to be adequately represented by $C = 1/Sc$, where in our studies of turbulent buoyant fires Sc is given by the turbulent Schmidt number for the scalar variance, i.e. $Sc_{T,Z''2}$. Unlike in RANS calculations, there are no transport equations to evaluate the quantities such as the SGS kinetic energy or its dissipation when it comes to a practical LES. Jiménez et al. [39] proposed nonetheless in employing the approximations of $\overline{k}$ and $\overline{\epsilon}$ derived from SGS turbulence models. By adopting the eddy viscosity model for the SGS stresses and the Yoshizawa model for the SGS kinetic energy given by

$$\overline{\varepsilon} = 2\left(\mu/\overline{\rho} + \mu_{\mathrm{T}}^{\mathrm{SGS}}/\overline{\rho}\right)\tilde{S}_{ij}\tilde{S}_{ij},\ \overline{k} = 2C''\Delta^2\tilde{S}_{ij}\tilde{S}_{ij} \tag{21}$$

the scalar dissipation $\tilde{\chi}$ is henceforth determined according to

$$\overline{\rho}\tilde{\chi} = \frac{(\mu + \mu_{\mathrm{T}}^{\mathrm{SGS}})}{Sc_{T,Z''2}C''\Delta^2}\widetilde{Z''^2} \tag{22}$$

which results in a well-conditioned expression, provided that the constants are not zero. Simulations performed by Jiménez et al. [39] have indicated that C'' varied from a value of 0.09 to a value of 0.06. Their investigations have revealed that dissipation could be accurately predicted both locally and on average when a constant intermediate value of 0.07 is adopted. Eq. (22) allows the formulation of appropriate forcing terms to represent dissipation and effects of mixing in the scalar variance evolution of which can be realized via the modelled transport equation. Following Jiménez et al. [39] proposal, the filtered source term $\overline{S}_{Z''^2}$ can be modelled according to

$$\overline{S}_{Z''^2} = 2\left(\frac{\mu}{Sc_{Z''^2}} + \frac{\mu_{\mathrm{T}}^{\mathrm{SGS}}}{Sc_{T,Z''^2}}\right)\frac{\partial\tilde{Z}}{\partial x_j}\frac{\partial\tilde{Z}}{\partial x_j} - \overline{\rho}\tilde{\chi} \tag{23}$$

Prior to running LES, the strategy is to purposefully construct a flamelet library for $\tilde{Y}_i(\tilde{Z},\widetilde{Z''^2},\tilde{\chi}_o)$. Firstly, $\tilde{Z}$ and $\widetilde{Z''^2}$ are chosen and $P(Z)$ is determined from Eq. (17). Secondly, $\tilde{\chi}_o$ is chosen. By assuming that the local subgrid fluctuation on χ_o to be negligible, which gives $\tilde{\chi}_o = \chi_o$, Eq. (12) is used to replace χ in the steady, species equation of the laminar flamelet model. This involves solving for the methane fuel as

$$\tilde{\chi}_o F(Z)\frac{\partial^2 Y_{\mathrm{F}}}{\partial Z^2} = \tilde{\chi}_o \exp\left(-2\left[\mathrm{erf}^{-1}(2Z-1)\right]^2 \right)\frac{\partial^2 Y_{\mathrm{F}}}{\partial Z^2} = \omega_{\mathrm{F}} \tag{24}$$

where ω_{F} is the Arrhenius chemical reaction rate which can be obtained from Westbrook and Dryer [40]. The mass species of the oxidant and product can be subsequently evaluated according to

$$Y_{\mathrm{O}} = (1-Z)Y_{\mathrm{O}_2} + r(Y_{\mathrm{F}} - ZY_{\mathrm{F1}}) \tag{25}$$

$$Y_{\mathrm{P}} = (r+1)(ZY_{\mathrm{F1}} - Y_{\mathrm{F}}) \tag{26}$$

where Y_{O_2} and Y_{F1} are the mass species of the oxidant and fuel at the respective free streams. With $P(Z)$ already known and solutions of $Y_i(Z,\tilde{\chi}_o)$ obtained from Eqs. (24)–(26), the filtered mass species $\tilde{Y}_i$ are then computed from Eq. (16). With the filtered scalar dissipation $\tilde{\chi}$ evaluated according to Eq. (12) during the LES computations, local peak value of $\tilde{\chi}_o$ is henceforth determined and alongside with calculated values of $\tilde{Z}$ and $\widetilde{Z''^2}$, the filter composition $\tilde{Y}_i$ is subsequently ascertained from the generated library of $\tilde{Y}_i(\tilde{Z},\widetilde{Z''^2},\tilde{\chi}_o)$. The filtered heat release rate can be accordingly evaluated through

$$\overline{\omega}_{\mathrm{T}} = \frac{1}{2}\overline{\rho}\tilde{\chi}\sum_{i=1}^{N}\int_{0}^{1} h_{\mathrm{f}i}^{\mathrm{o}}\frac{\mathrm{d}^2 Y_i}{\mathrm{d}Z^2}P(Z)\mathrm{d}Z \tag{27}$$

2.2. Soot formation and radiation models

Our investigations employing RANS approaches for compartment fires [12,41,42] have revealed that soot particles contributed significantly in augmenting the overall radiative heat transfer within the enclosures from a fire. Tracking the evolution of soot volume fraction is thereby essential in the current study. The two-equation semi-empirical soot model by Moss et al. [43] that incorporates the essential physical processes of soot nucleation, coagulation and surface growth is adopted. This model is attractive as it describes the soot production simply in terms of the local temperature and mole fraction of fuel.

The filtered soot source terms of $S_{\zeta_{\mathrm{n}}}$ and $S_{\zeta_{\mathrm{s}}}$ are closed in terms of the filtered composition and filtered temperature, thus neglecting some of the effects of SGS fluctuations on these terms. Hence, soot production is determined predominantly by the large-scale turbulent advection, SGS turbulent diffusion and finite-rate soot chemistry effects. For the soot formation, the soot particulate number density source term $S^{+}_{\zeta_{\mathrm{n}}}$ is expressed by:

$$S^{+}_{\zeta_{\mathrm{n}}} = \overline{\alpha} - \overline{\rho}^2\overline{\beta}\tilde{\zeta}_{\mathrm{n}}^2 \tag{28}$$

whilst the soot volume fraction source term $S^{+}_{\zeta_{\mathrm{s}}}$ is given as:

$$S^{+}_{\zeta_{\mathrm{s}}} = \overline{\delta} - N_{\mathrm{o}}^{1/3}\overline{\rho\gamma}\tilde{\zeta}_{\mathrm{s}}^{2/3}\tilde{\zeta}_{\mathrm{n}}^{1/3} \tag{29}$$

The rate of particle nucleation is given by $\overline{\alpha} = C_\alpha\overline{\rho}^2\tilde{T}^{1/2}\tilde{X}_{\mathrm{fu}}\exp(-T_{\mathrm{a}}/\tilde{T}) = \overline{\delta}/144$ where $\tilde{X}_{\mathrm{fu}}$ is the filtered fuel mole fraction. The coagulation of soot is described by Smoluchowski expression [44]: $\overline{\beta} = C_\beta\tilde{T}^{1/2}$. The last term in Eq. (29) represents the surface growth of soot suggested by Syed et al. [45] which contained a linear dependence on aerosol surface area, and is controlled by the rate relationship: $\overline{\gamma} = C_\gamma\overline{\rho}\tilde{T}^{1/2}\tilde{X}_{\mathrm{fu}}\exp(-T_\gamma/\tilde{T})$. The Nagle and Strickland-Constable rate [46] for soot oxidation is adopted as the limiting mechanism for oxidation by O_2. Denoting $\overline{P}_{\mathrm{O}_2}$ as the filtered partial pressure of O_2, the overall reaction rate ($\mathrm{kg\,m^{-2}\,s^{-1}}$) is given by

$$\overline{R}_{\mathrm{ox}} = 120\left[\frac{k_{\mathrm{A}}\overline{P}_{\mathrm{O}_2}}{1+k_Z\overline{P}_{\mathrm{O}_2}}\chi + k_{\mathrm{B}}\overline{P}_{\mathrm{O}_2}(1-\chi)\right] \tag{30}$$

where

$$\chi = \frac{1}{1+(k_{\mathrm{T}}/(k_{\mathrm{B}}\overline{P}_{\mathrm{O}_2}))} \tag{31}$$

and

$$k_{\mathrm{A}} = 2\times10^4\exp\left(-\frac{30,000}{R_{\mathrm{u}}\tilde{T}}\right) \tag{32}$$

$$k_{\mathrm{B}} = 4.46\exp\left(-\frac{15,200}{R_{\mathrm{u}}\tilde{T}}\right) \tag{33}$$

$$k_{\mathrm{T}} = 1.51\times10^8\exp\left(-\frac{97,000}{R_{\mathrm{u}}\tilde{T}}\right) \tag{34}$$

$$k_Z = 2.13\times10^4\exp\left(\frac{4100}{R_{\mathrm{u}}\tilde{T}}\right) \tag{35}$$

It is noted that the units for the above reaction rate constants are in kg, m, s, cal, K, atm. The local particulate number density and soot volume fraction are reduced by combustion according to

$$S^{-}_{\zeta_{\mathrm{n}}} = -N_{\mathrm{o}}^{1/3}\left(\frac{36\pi}{\rho_{\mathrm{soot}}^2}\right)^{1/3}\frac{\overline{\rho}\overline{R}_{\mathrm{ox}}\tilde{\zeta}_{\mathrm{n}}^{4/3}}{\tilde{\zeta}_{\mathrm{s}}^{1/3}} \tag{36}$$

$$S^{-}_{\zeta_{\mathrm{s}}} = -N_{\mathrm{o}}^{1/3}\left(\frac{36\pi}{\rho_{\mathrm{soot}}^2}\right)^{1/3}\overline{\rho}\overline{R}_{\mathrm{ox}}\tilde{\zeta}_{\mathrm{n}}^{1/3}\tilde{\zeta}_{\mathrm{s}}^{2/3} \tag{37}$$

Hence, the net rate source terms for the local particulate number density and soot volume fraction are evaluated according to

$$S_{\zeta_{\mathrm{n}}} = S^{+}_{\zeta_{\mathrm{n}}} + S^{-}_{\zeta_{\mathrm{n}}} \tag{38}$$

$$S_{\zeta_{\mathrm{s}}} = S^{+}_{\zeta_{\mathrm{s}}} + S^{-}_{\zeta_{\mathrm{s}}} \tag{39}$$

Appropriate values for the pre-exponential constants C_α, C_β and C_γ and activation temperatures T_α and T_β for methane are obtained from Syed et al. [45], *viz.*,

$C_\alpha = 65400\ \mathrm{m^3\,kg^{-2}\,K^{-1/2}\,s^{-1}}$
$C_\beta = 1.3\times10^7\ \mathrm{m^3\,K^{-1/2}\,s^{-1}}$
$C_\gamma = 0.1\ \mathrm{m^3\,kg^{-2/3}\,K^{-1/2}\,s^{-1}}$
$T_\alpha = 46100\ \mathrm{K}$
$T_\gamma = 12600\ \mathrm{K}$

Luminous thermal radiation from combustion products and soot is treated by solving the filtered radiative transfer equations (FRTE) for a non-scattering grey gas using the Discrete Ordinates Method (DOM) with S_4 quadrature scheme [47]. The grey gas assumption and the S_4 approximation allow for more efficient computations. The discrete radiative transfer equation is spatially filtered resulting in the following FRTE shown below for a Cartesian coordinate system in three dimensions:

$$\xi_j\frac{\partial\overline{I}_j}{\partial x} + \eta_j\frac{\partial\overline{I}_j}{\partial y} + \zeta_j\frac{\partial\overline{I}_j}{\partial z} \approx \overline{K}_{\mathrm{a}}(E_{\mathrm{b}} - \overline{I}_j) \tag{40}$$

In this present investigation, Eq. (40) neglects the interaction of the SGS turbulence-radiation. The blackbody radiation is defined as $E_{\mathrm{b}} = \sigma\tilde{T}^4$. The direction cosines ξ_j, η_j and ζ_j represent a set of directions for each of the radiation intensities $\overline{I}_j$ that span over the total solid angle range of 4π around a point in space. The integrals over solid angles are approximated using the S_4 numerical quadrature where the maximum number of discrete ordinates is 24. The discrete version of the radiation source term S_{rad} that appears in the filtered energy equation is:

$$S_{\mathrm{rad}} \approx -4\overline{K}_{\mathrm{a}}E_{\mathrm{b}} + \sum_{j=1}^{24} w_j\overline{K}_{\mathrm{a}}\overline{I}_j\left(\widehat{s}_j\right) \tag{41}$$

The filtered gas absorption coefficient ($\overline{K}_{\mathrm{a,g}}$) for the combustion products (CO_2 and H_2O) as well as the unburnt methane fuel can be approximated according to the Weighted Sum of Gray Gases Model (WSGGM) according to Beer et al. [48], which considers a one-clear two-gray gases representation similar to the consideration proposed by Truelove [49]. For soot, the expression from Kent and Honnery [50] is employed: $\overline{K}_{\mathrm{a,s}} = 1864\tilde{f}_{\mathrm{v}}\tilde{T}$. The absorption coefficient in Eq. (41) is evaluated based on the sum of the filtered gas and soot absorption coefficients, i.e. $\overline{K}_{\mathrm{a}} = \overline{K}_{\mathrm{a,g}} + \overline{K}_{\mathrm{a,s}}$.

3. Numerical details

3.1. Numerical methods

The finite volume method is employed to discretize the above filtered governing equations on a collocated gird. Second-order central differencing is adopted for all spatial derivatives approximations. The solution advancements in the time space of Eqs. (1)–(3) are achieved numerically by using the predictor–corrector approach [22]. The approach involves a second-order Adams–Bashforth time integration scheme for predictor stage follow by a second-order quasi Crank–Nicolson integration for the corrector stage. Moreover, for the evolution of soot formation, time derivatives of soot quantities are solved numerically by using a fourth-order Runge-Kutta scheme.

Through the predictor–corrector approach, strong coupling effects between the density and fluid flow equations, which contributes to the baroclinic vorticity generation, can be resolved. A pressure correction step was incorporated in both predictor and corrector by involving the inversion of a pressure correction Poisson equation, which is solved using Krylov methods as Eq. (42).

$$\left(\overline{\rho}^{*}\tilde{u}_j'\right)_{\mathrm{f}} = \left(\rho^n \tilde{u}_j^n\right)_{\mathrm{f}} + \Delta t\left[\frac{3}{2}R_{i,\mathrm{f}}^n - \frac{1}{2}R_{i,\mathrm{f}}^{n-1} - \left(\frac{\partial \overline{p}^n}{\partial x_j}\right)_{\mathrm{f}}\right] \tag{42}$$

The terms represented by $(\rho^n \tilde{u}_j^n)_{\mathrm{f}}$, $R_{i,\mathrm{f}}^n$ and $R_{i,\mathrm{f}}^{n-1}$ can simply be obtained by linear interpolation whilst the face pressure gradient $(\partial \overline{p}^n/\partial x_j)_{\mathrm{f}}$ is approximated by a second-order central difference between the cell centres. This interpolation technique resembles very closely to the Rhie–Chow methodology [51]. Numerical details of the predictor–corrector approach can be found in our previous publication [22] and the references therein.

3.2. Computational domain and boundary condition

Numerical simulation was conducted of a large-scale (i.e. 1 m in fire bed diameter) methane pool fire experiment of Tieszen et al. [22]. A square cube computational domain of 3 m length was employed for the simulation. A methane fuelled burner with 1 m diameter was centrally placed on the floor level of the domain. A methane inlet velocity of 9.7 cm/s was specified at the burner corresponding to the fire of 2.07 MW heat release rate measured in the experiment. McGrattan et al. [52] indicated that the characteristic length scale of a fire plume structure can be related to the total heat release rate $\dot{Q}$ (W) by Eq. (43).

$$L^{*} = \left(\frac{\dot{Q}}{\rho_{\mathrm{ref}} T_{\mathrm{ref}} C_p \sqrt{g}}\right)^{2/5} \tag{43}$$

For the heat release considered in this present investigation, the characteristic length L^{*} is approximately in the order of 1.3 m. Based on our preliminary, two non-uniform mesh distributions of $96 \times 96 \times 96$ and $116 \times 116 \times 116$ cells were overlaid within the computational domain with finer grid cells centred above the burner to better capture all the necessary macroscopic large-scale features of the flaming fire. No significant difference of the predicted results was observed when simulations were performed on the two grid resolutions. For the best trade-off between numerical accuracy and cost, the non-uniform mesh of 96^3 cells with the minimum spacing of 1.4 cm above the burner was thus employed in this paper. The traction-free boundary condition was employed for all lateral boundaries [53]. For the top boundary, a zero gradient condition was imposed for all the transport variables. To prevent

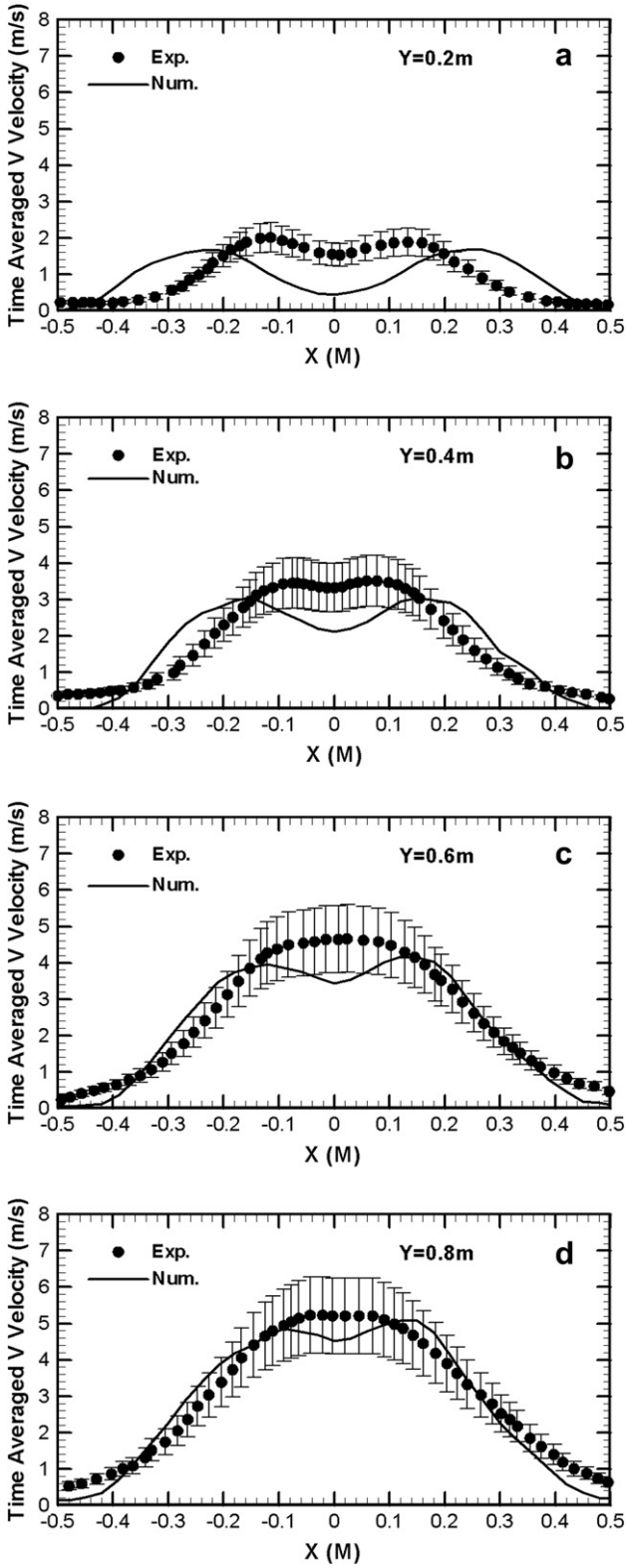

Fig. 2. Predicted and measured time-averaged vertical velocity at different centre-line locations: (a) $Y = 0.2$ m; (b) $Y = 0.4$ m; (c) $Y = 0.6$ m and (d) $Y = 0.8$ m.

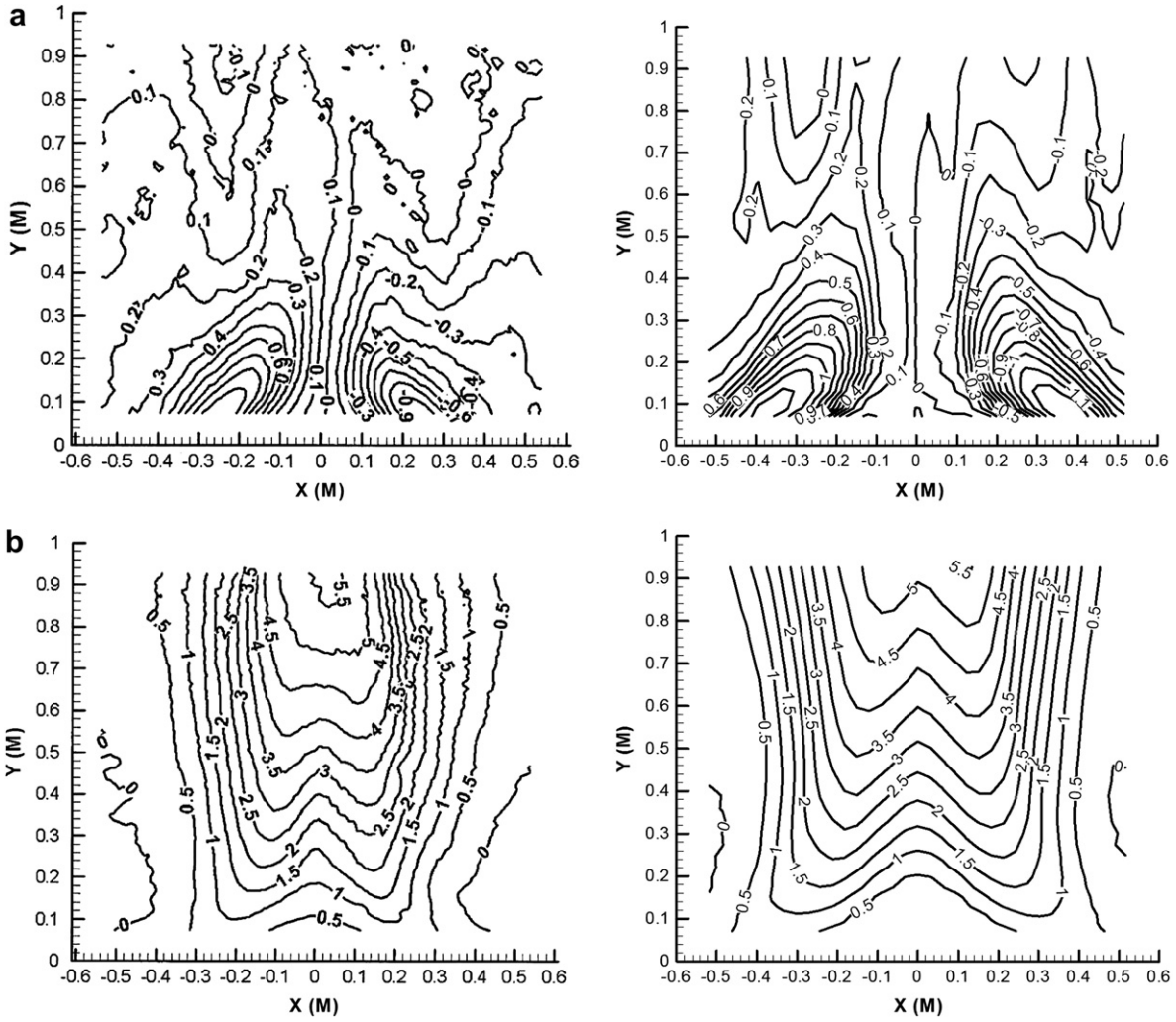

Fig. 3. Comparison of time-averaged velocity component contours captured from PIV measurement of Tieszen et al. [20] (left column) and the present LES model (right column) at the centre-plane of the fire: (a) *U* velocity (horizontal) and (b) *V* velocity (vertical).

flow entering into domain at the top which might incur numerical instabilities, velocities with negative values were forced to zero.

4. Results and discussions

A transient analysis was performed with approximately 44,000 time steps for the numerical simulation of buoyant plume. Stable time-stepping was accomplished through the acoustic CFL condition. The time step was determined by employing a CFL number of 0.35 to achieve time-accurate solution via:

$$\mathrm{d}t = 0.35/\left(\max\left(\left|\frac{u}{\Delta x}\right| + \left|\frac{v}{\Delta y}\right| + \left|\frac{w}{\Delta z}\right|\right)\right) \tag{44}$$

4.1. Time-averaged velocity, turbulent quantities and temperature distribution

A quasi-steady state solution was obtained when the physical time arrived at 35 s. Time-averaged field quantities were then extracted by performing time-weighted averaging calculation over 10 s of instantaneous solutions. Fig. 2 illustrates the predicted and measured time-averaged vertical velocity profiles at different centre-line locations (i.e. $Y = 0.2$, 0.4, 0.6 and 0.8 m) above the methane burner. In general, the predicted velocity profiles agreed reasonably well with the measurement. Especially at the location $Y = 0.8$ m, the maximum error of prediction is 13% which is well within the ±20% uncertainly bounds of the measurements. Larger discrepancies were observed at the vicinity of burner surface (i.e. $Y = 0.2$ and $Y = 0.4$) in Fig. 2a and b. As predicted in the figures, the distance between two velocity peaks was considerably over-predicted. A more comprehensive depiction could be found in Fig. 3 where time-averaged horizontal and vertical velocity contour plots were compared with measured results. Overall, the predicted time-averaged velocity contours of the present fully-coupled LES model are in good agreement with the measurements. In Fig. 3a, aligned with the observation in Fig. 2, the predicted gap between two velocity regions can be observed to be wider than measurement. This suggested that the present model slightly over-estimated the spreading rate of velocities and the width of the fire plume as evident in vertical contours shown in Fig. 3b.

Similar numerical errors were also reported by Rawat et al. [18] and Desjardin [19] where they both concluded that these numerical errors were attributed to the insufficient grid resolution for LES models to resolve the microscopic baroclinic vorticity generation near the burner surface. As this mechanism was observed to be

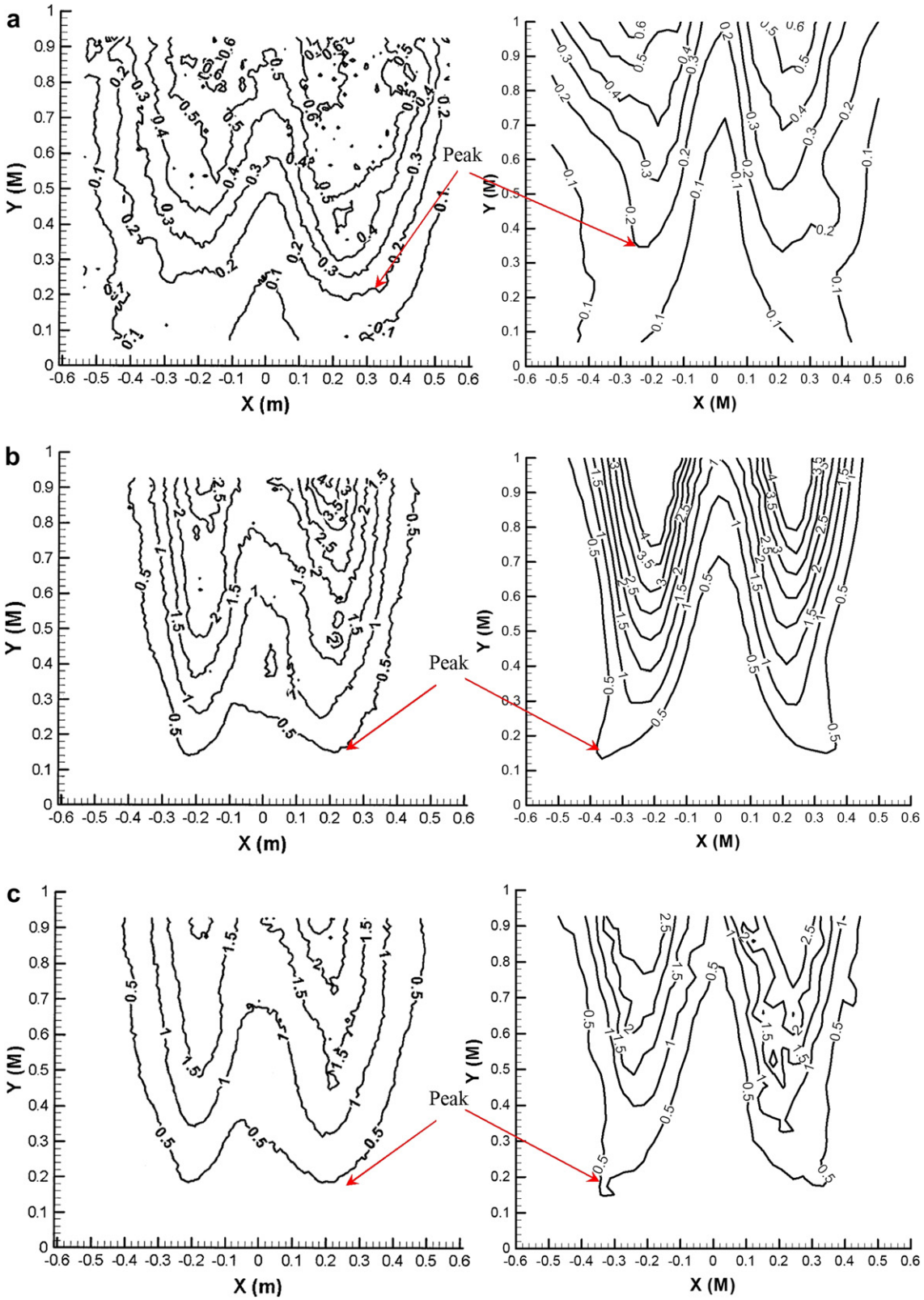

Fig. 4. Comparison of time-averaged of velocity fluctuations and turbulent kinetic energy contours captured from PIV measurement of Tieszen et al. [20] (left column) and the present LES model (right column) at the centre-plane of the fire: (a) the square of horizontal velocity fluctuation, $\overline{u'^2}$; (b) the square of horizontal velocity fluctuation, $\overline{v'^2}$ and the turbulent kinetic energy, k.

responsible for the sequential up-scale turbulent energy transfer to large-scale eddies, filtering of these small-scale turbulent motions by the LES models might cause under-prediction of the local turbulent mixing rate resulting in an inaccurate estimation of the local heat release, combustion and velocity spread rates. Resolving these microscopic scales requires performing DNS at the base of the

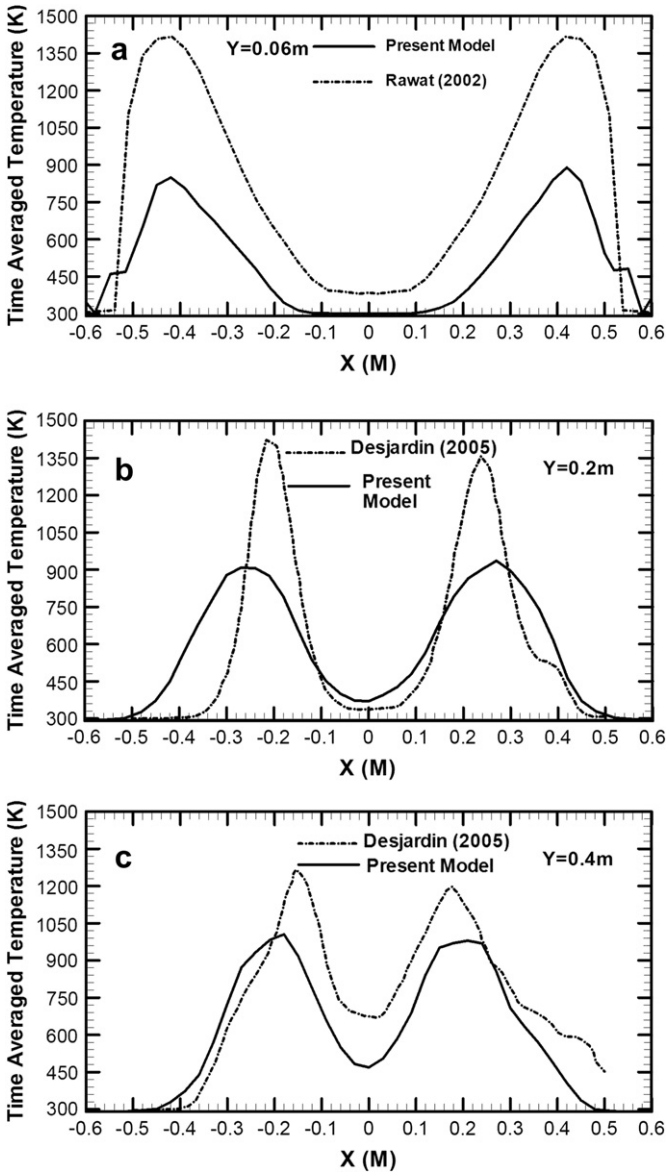

Fig. 5. The predicted time-averaged temperature profiles in comparison to numerical results of Rawat et al. [18] and Desjardin [19] at different centre-line locations: (a) $Y = 0.06$ m; (b) $Y = 0.2$ m and (c) $Y = 0.4$ m.

plume with significant burden to both computational time and resources. The above pulsation could be further ascertained by comparing the predicted and measured time-averaged turbulent quantities distribution at centre-plane of the fire plume as shown in Fig. 4. As depicted, especially for the turbulent kinetic energy, turbulent quantities were slightly under-estimated at the centre of burner surface. Away from this region, all turbulent quantities are in good quantitative agreement with the experiment data. Locations of the peaks of these turbulent quantities are successfully captured. Furthermore, the single-step combustion reaction assumption adopted in the numerical simulation could be another source of error coupling with the velocity field.

Without any temperature measurements being made in the experiment of Tieszen et al. [20], a thorough validation between numerical and experimental temperature profiles is not made possible. We compare however our predicted time-averaged temperature profiles against the numerical results reported individually by Rawat et al. [18] and Desjardin [19] at different centre-line locations (i.e. $Y = 0.06$, 0.2 and 0.4 m) above the burner such as shown in Fig. 5. Our predicted temperatures followed similar trends with other simulation results. However, the flame temperatures appeared in lower values than others especially at the local temperature peaks. Although no comment can be made on the accuracy of all results with the absence of experimental data, such discrepancies could be contributed by the differences in the physical models employed during numerical simulations. The major differences could be due to absence of soot and radiation models that are required to be deployed In Desjardin [19], soot formation and its augmentation to the global radiative heat transfer were neglected. By accounting soot particles and radiation heat loss in our simulation, it is expected that temperatures would be relatively lower than Desjardin's results. On the other hand, Rawat et al. [18] employed a detailed chemistry approach in their flamelet combustion and soot formation calculation. A simple M_1 radiation model was however adopted by Rawat et al. [18] and they concluded that the M_1 radiation model might under-estimated the radiation emission from the pool fire and consequently over-predicted the local flame temperatures and vertical velocity.

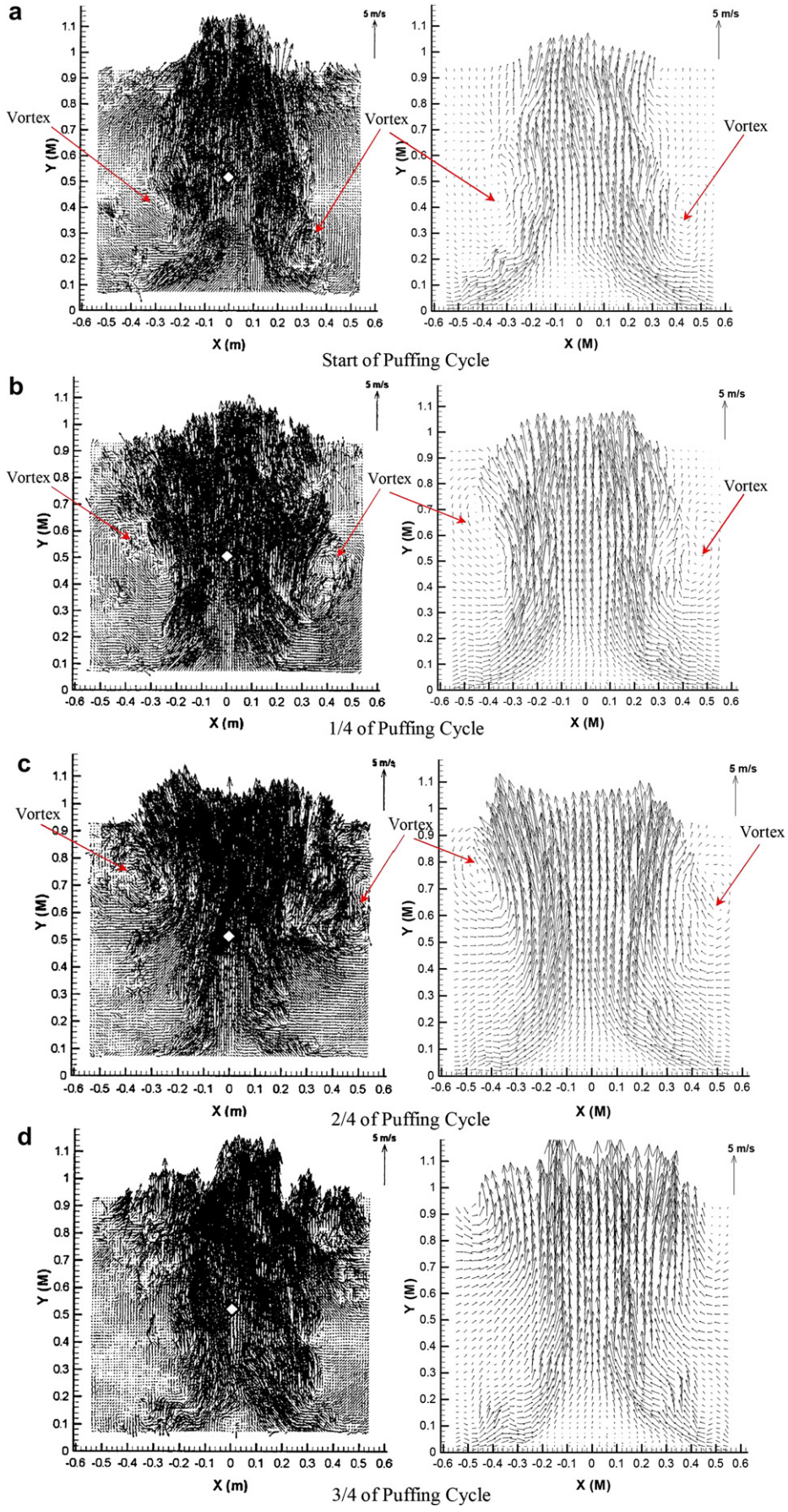

Fig. 6. Four instantaneous velocity field at the centre-plane of the fire plume captured by PIV measurement of Tieszen et al. [20] (left column) and the present LES model (right column): (a) start; (b) 1/4; (c) 2/4 and (d) 3/4 of puffing cycle.

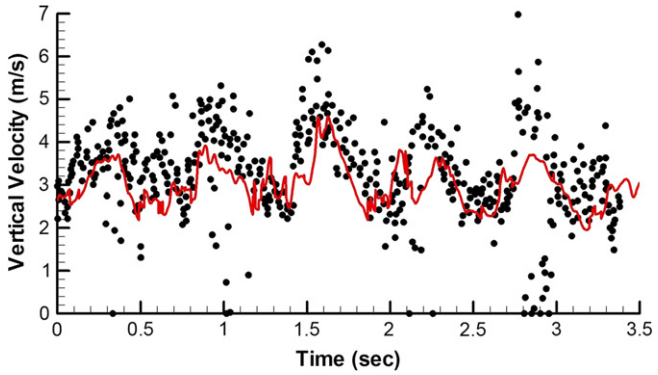

Fig. 7. Time history of the vertical velocity at the centre-point of fire ($X = 0$, $Y = 0.505$) predicted by present model (line) and recorded by PIV measurement (points).

Nonetheless, it should be emphasised that some assumptions which could affect temperature predictions have also been incorporated in the present model. Within our soot calculation, based on the single-step combustion assumption, the unburnt fuel (methane) was assumed as the soot precursor of the whole soot formation processes. According to Frenklach and Wang [54], soot formation is mainly initialized by the presence of acetylene (i.e. C_2H_2) and follows by a sequence of polycyclic aromatic hydrocarbon (PAH) formation and oxidation processes. Using the parent fuel as soot precursor might tend to over-predict the soot volume fraction and the associated radiation heat loss from fire. The corresponding temperature and velocity predictions were thereby under-predicted (as shown in Fig. 2). This also explained the temperature discrepancy between Rawat's and our simulation results.

4.2. Instantaneous velocity fields and time history of vertical velocity

The temporal vortical structures and its coupled combustion behaviour of the large-scale pool fire are discussed herein. Fig. 6 shows the instantaneous velocity field at the centre-plane of the fire plume captured by the PIV measurement of Tieszen et al. [20] and the present LES model. The four sequential PIV results on the left column clearly illustrated the relationship between large vortical structures and the puffing cycle. At the start of the cycle, turbulent eddies were firstly stemmed from the base of the fire which has been caused by baroclinic vorticity generation. Owing to the amalgamation of eddies and buoyancy forces, the size of vortical structures continuously increased and accelerated in the vertical direction until it has been advected out of the image (see Fig. 6b, c). In comparison to the PIV measurements, four sequential predicted vector plots were also extracted within one arbitrary puffing cycle from the present model (as shown in the right column of Fig. 6). A broad overview of the figure suggested that the predicted instantaneous velocity fields were in excellent agreement with the PIV measurements.

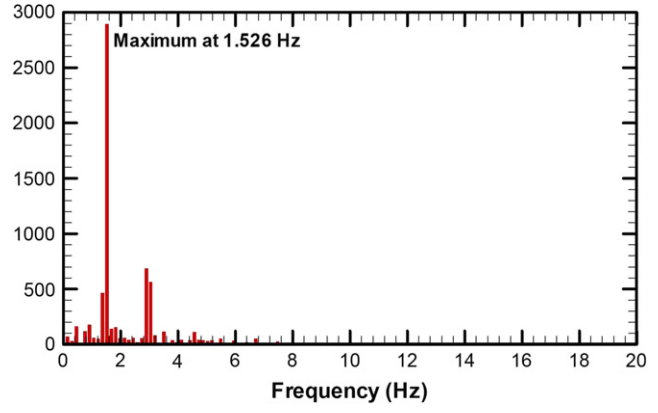

Fig. 8. Frequency spectrum of the time history line in Fig. 7 obtained by Fast Fourier Transform (FFT).

Velocity vectors of predicted results also exhibited a similar behaviour/distribution to the experimental data. Special attention was paid on the simulated vortical structures at both sides of the fire. As depicted in the figure, the vortical structures were successfully captured by the present model. From the start to the end of puffing cycle, the simulated vortical structures were created at the fire base and continuously developed in size and convected upward away through the top of plot. The above development of the vortices was clearly aligned with the observations of PIV measurements. Vortex locations of the numerical results were also comparable to the measurement.

In connection with the above qualitative comparison, a closer examination of the pulsating behaviour of the pool fire can be analysed by tracing the time history of the vertical velocity at the centre-point of fire ($X = 0$, $Y = 0.505$ m) in comparison to the record of PIV measurement in Fig. 7. As summarized in Tieszen et al. [20], the PIV record indicated that the periods of the puffing cycles preserved a somewhat regular pattern but varied slightly from time to time. In general, the predicted vertical velocity history exhibited similar pattern with the measurement. Nevertheless, it must be confessed that the predicted time history line appears much "smoother" than the scattering measurement points where a more chaotic behaviour and sharp peaking of the velocity fluctuations have been observed. Such smoothing effect on the numerical results was contributed by the nature of the LES models. Based on the spatial filtering technique, LES models only resolve large eddy motions above the subgrid length. Subgrid scale eddy motions were filtered and modelled by the SGS model. Re-capturing these chaotic flow behaviours would require significant improvement of the current grid resolution or even Direct Numerical Simulation scheme which demands excessive computational resources. Fig. 8 illustrates the frequency spectrum obtained from above time history line of instantaneous vertical velocity by Fast Fourier Transform (FFT). The figure clearly shows a dominant frequency at 1.526 Hz which is only 8% faster than the measured pulsation frequency (1.65 Hz). Based on the above thorough quantitative comparison, it can be concluded that the present LES model is capable to resolve the temporal effects from the vortical structures and its resultant pulsation frequency of large-scale pool fire.

4.3. Instantaneous temperature and soot level distributions

Fig. 9 shows the instantaneous temperature contour at the centre-plane of the fire and the temperature iso-surfaces plots captured at the same puffing cycle of the vector plots as shown in Fig. 6. From the figure, coupling effect of the vortical structures and chemical combustion processes can be revealed. At the start of the puffing cycle, vortical structures were generated at the fire base. These vortex motions assisted the air entrainment into the reaction zone causing high local temperatures in both sides as shown in Fig. 9a. The increased air entrainment also created the characteristic "necking" at bottom of the fire plume. Consequently, buoyancy forces formed by high local temperatures pushed the vortical structures upward, which in turn created a low pressure region filling up by a "bulge" of combustion gases (see Fig. 9b, c). These combustion gases then underwent further chemical reactions creating high local temperatures and pushed the vortices upward to higher level as shown in Fig. 9d.

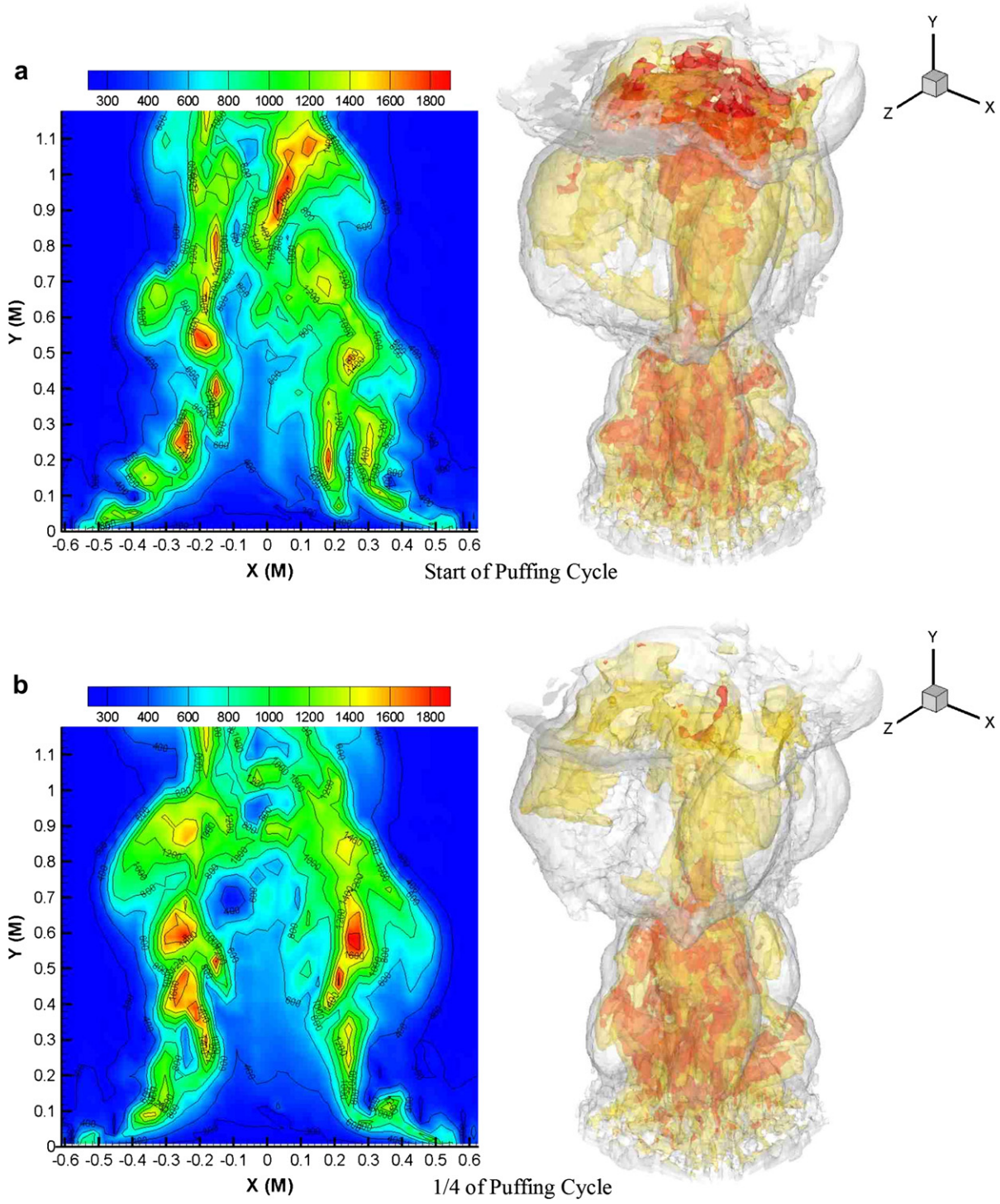

Fig. 9. Instantaneous temperature contour plots at the centre-plane of the fire and the temperature iso-surfaces captured at the same puffing cycle of the vector plots as shown in Fig. 6; 800 K (visible flame in red), 450 K (flame tips in yellow) and 310 K (cold smoke in grey). (For interpretation of the references to colour in figure legends, the reader is refered to the web version of this article.)

A clearer picture showing the three-dimensional propagation of vortical structures within the whole computational domain can be observed from the temperature iso-surface plots on right column of Fig. 9. The figure clearly illustrates the coherent vortex structures and its propagation in both vertical and transverse directions. In comparison with other observations [4–6], these large vortical structures were almost symmetric and appeared as completed rings (also referred as smoke/fire balls). As depicted in the figure, throughout the puffing cycle, the length scale of vortical ring structures were formed initially of similar order with the burner base and continuously grow in size while travelling upward by buoyancy. This flow behaviour was also observed by Tieszen et al. [6] based on a series of photographs taken from various large-scale fire experiments.

Fig. 10 shows the instantaneous soot level distribution at the centre-plane of the fire captured at the same puffing cycle

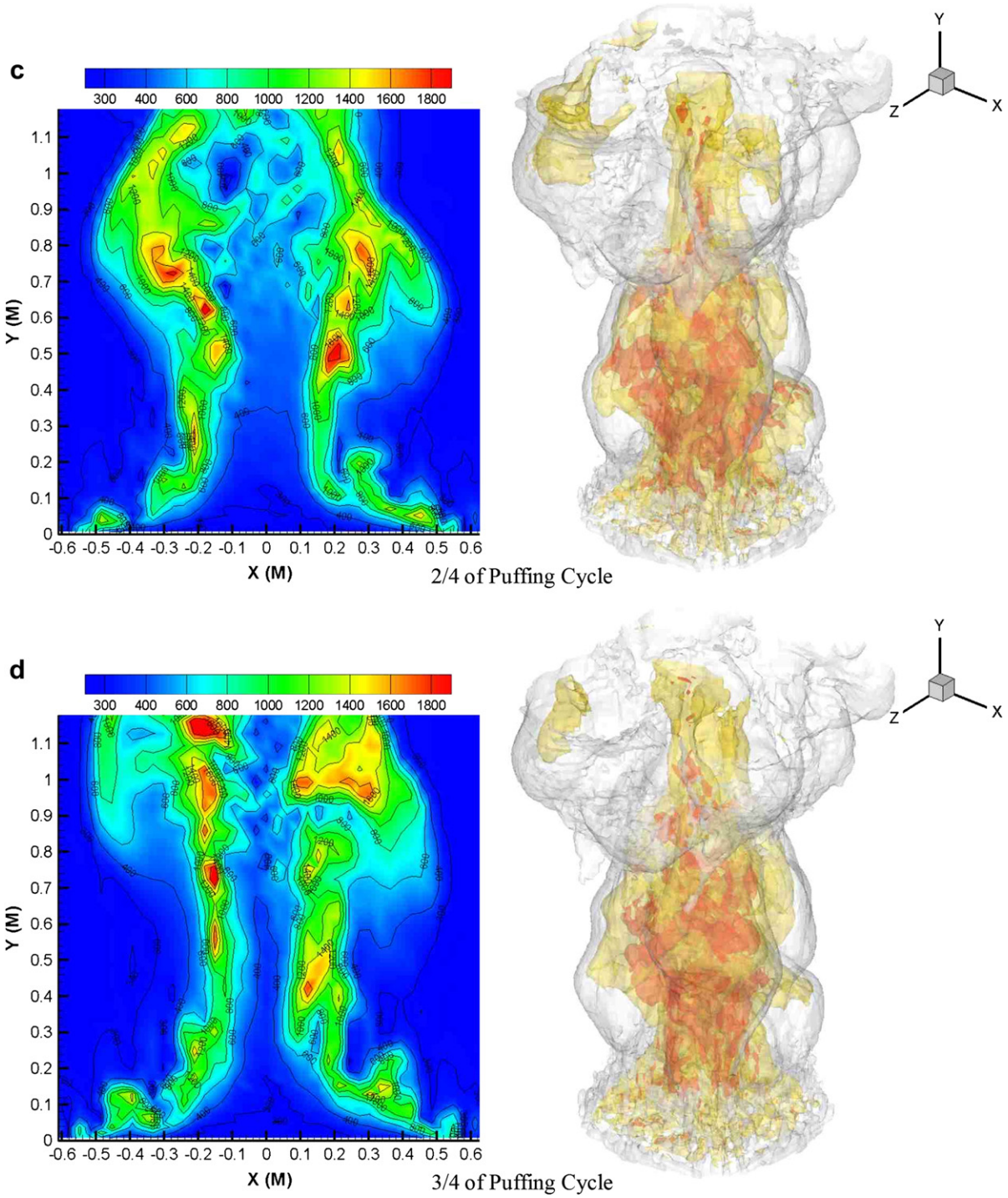

Fig. 9. (*continued*).

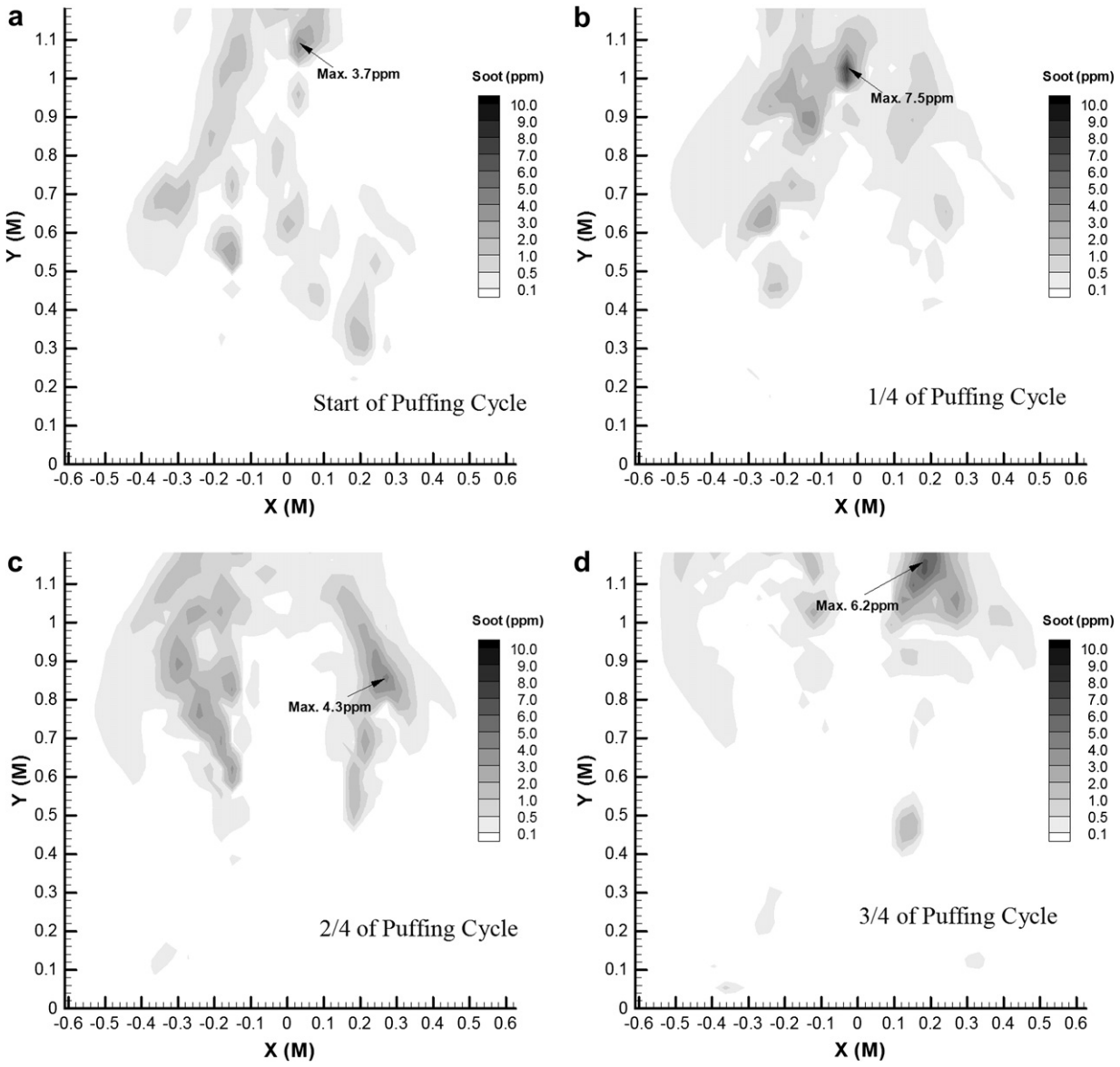

Fig. 10. Instantaneous soot level distribution at the centre-plane of the fire captured at the same puffing cycle of the vector plots as shown in Fig. 6.

of the vector plots as shown in Fig. 6. As depicted, majority of the soot particles were concentrated at the upper part of the fire plume with its maximum level ranged from 3 to 7 ppm. Based on the latest measurement of a 7.1 cm diameter methane buoyant flame by Xin and Gore [55], the maximum soot level was found to be around 5 ppm. As a heavier sooting 1 m diameter pool fire is being considered in this study, the predicted maximum soot level is consistent with the experimental measured level.

5. Conclusions

A numerical study simulating the temporal vortical structures of a large-scale buoyant pool fire has been carried out using a fully-coupled LES model which incorporated all essential turbulence, combustion, radiation and soot chemistry considerations. Based on the strained laminar flamelet approach, an SGS combustion model with conditional scalar dissipation rate was developed in order to provide a more comprehensive description of highly non-equilibrating burn and extinguishment of flamelets occurring in pool fires. The time-averaged velocity, turbulent fluctuation quantities and temperature profiles from the present model were in good agreement in comparison to experiment data and other numerical results. Instantaneous vector plots were compared alongside with PIV measurements. The predicted velocity magnitudes and vortex locations were found to be qualitatively comparable with experimental data suggesting that the simulation is capable reproducing the typical temporal and spatial evolution of the large-scale vortical structures and its puffing behaviour of buoyant pool fire. Quantitative validations of the time history of velocity fluctuations and the pulsation frequency were also presented with excellent agreement with experimental data. Contours and iso-surfaces of instantaneous temperature distributions were included to illustrate the transient behaviour of vortices propagation. Comparing with the observations by Tieszen et al. [6], these plots demonstrated that the large-scale vortices appeared in almost symmetric completed fire/smoke rings propagated continuously upward with the initial length scale in similar order of the burner base. Furthermore, contours of instantaneous soot level distributions were also included and the predicted maximum soot level was found consistent with the

experimental observation by Xin and Gore [55]. The above encouraging results clearly demonstrated the capability of the fully-coupled LES model in capturing the pulsation behaviour of large-scale pool fire. Nonetheless, from the numerical viewpoint, one should be noticed that some assumptions were inevitably adopted to simplify the solution procedures of the model. One of the main simplifications comes from the single-step reaction scheme. Based on this assumption, concentrations of intermediate chemical species (e.g. acetylene/benzene) were not explicitly solved within the simulation. Incorporating the detailed/reduced chemistry consideration into the reaction scheme could be one of the development directions extending the model to account more comprehensive combustion/soot formation scheme in future study.

Acknowledgement

The financial support provided by the Australian Research Council (ARC project ID LP0882413) is also gratefully acknowledged.

References

[1] D. Drysdale, in: An Introduction to Fire Dynamics, second ed. Wiley, New York, 1999.
[2] G.M. Bryan, R.M. Nelson, The modelling of pulsating fires, Fire Technol. 6 (1970) 102–110.
[3] R. Portscht, Studies on characteristic fluctuations of the flame radiation emitted by fires, Combust. Sci. Technol. 10 (1975) 73–84.
[4] B.J. McCaffrey, Momentum implications for buoyant diffusion flames, Combust. Flame 52 (1983) 149–167.
[5] E.E. Zukoski, B.M. Cetegen, K. Kubota, Visible structures of buoyant diffusion flames, in: Proceedings of the 20th Symposium (International) on Combustion, The Combustion Institute, 1984, pp. 361–366.
[6] S.R. Tieszen, V.F. Nicolette, L.A. Gritzo, J.K. Holen, D. Murray, J.L. Moya, Vortical structure in pool fires: observation, speculation and simulation, Sandia Report 96-2607, Sandia Laboratory, 1996.
[7] W.E. Mell, K.B. Mcgrattan, H.R. Baum, Numerical simulation of combustion in fires, in: Proceedings of 26th Symposium (International) on Combustion, The Combustion Institute, 1996, pp. 1523–1530.
[8] X. Jiang, K.H. Luo, Direct numerical simulation of the puffing phenomenon of an axisymmetric thermal plume, Theor. Comput. Fluid Dyn. 14 (2001) 55–74.
[9] K.T. Yang, Recent development in field modelling of compartment fires, JSME Int. J. Ser. B 37 (1994) 702–717.
[10] A.N. Beard, Fire modelling and design, Fire Safety J. 28 (1997) 117–138.
[11] J.B. Moss, C.D. Stewart, Flamelet-based smoke properties for the field modelling of fires, Fire Safety J. 30 (1998) 229–250.
[12] S.C.P. Cheung, R.K.K. Yuen, G.H. Yeoh, G.W.Y. Cheng, Contribution of soot particles on global radiative heat transfer in a two-compartment fire, Fire Safety J. 39 (2004) 412–428.
[13] Y. Xin, J.P. Gore, K.B. Mcgrattan, R.G. Rehm, H.R. Baum, Large eddy simulation of buoyant turbulent pool fires, in: Proceedings of 29th Symposium (International) on Combustion, The Combustion Institute, 2002, pp. 259–266.
[14] Y. Xin, J.P. Gore, K.B. Mcgrattan, R.G. Rehm, H.R. Baum, Fire dynamic simulation of a turbulent buoyant flame using a mixture fraction-based combustion model, Comb. Flame 141 (2005) 329–335.
[15] K.B. McGrattan, G. Forney, Fire Dynamics Simulator (Version 4) – User's Guide, NIST Special Publication 1019, National Institute of Standard and Technology, 2004.
[16] Y. Kang, J.X. Wen, Large eddy simulation of a small pool fire, Combust. Sci. Technol. 176 (2004) 2193–2223.
[17] H.R. Baum, K.B. McGarttan, R.G. Rehm, Simulation of smoke pressure from large pool fire, in: Proceedings of 25th Symposium (International) on Combustion, The Combustion Institute, 1994, pp. 1463–1469.
[18] R. Rawat, H. Ptisch, J.F. Ripoll, Large-eddy simulation of pool fires with detailed chemistry using an unsteady flamelet model, in: Proceedings of the Summer Program 2002, Center for Turbulence Research, Stanford University, 2002.
[19] P.E. Desjardin, Modeling of conditional dissipation rate for flamelet models with application to large eddy simulation of fire plumes, Comb. Sci. Technol. 177 (2005) 1883–1916.
[20] S.R. Tieszen, T.J. O'hern, R.W. Schefer, E.J. Weckman, T.K. Blanchat, Experimental study of the flow field in and around a one meter diameter methane fire, Comb. Flame 129 (2002) 378–391.
[21] J.X. Wen, K. Kang, T. Donchev, J.M. Karwatzki, Validation of FDS for the prediction of medium-scale pool fire, Fire Safety J. 42 (2007) 127–138.
[22] S.C.P. Cheung, G.H. Yeoh, A.L.K. Cheung, R.K.K. Yuen, Flickering behaviour of turbulent buoyant fires using large-eddy simulation, Num. Heat Transf. Part A 52 (2007) 679–712.
[23] A.L.K. Cheung, E.W.M. Lee, R.K.K. Yuen, G.H. Yeoh, S.C.P. Cheung, Capturing the pulsation frequency of a buoyant pool fire using the large eddy simulation approach, Num. Heat Transf. Part A 53 (2008) 561–576.
[24] B.J. McCaffrey, Purely Buoyant Diffusion Flames: Some Experimental Results, NBSIR (National Institute of Standard and Technology), 1979.
[25] H.R. Baum, B.J. McCaffrey, Fire induced flow field-theory and experiment, fire safety science, in: Proceedings of Second International Symposium, 1989, pp. 129–148.
[26] Y. Xin, S.A. Filatyev, K. Biswas, J.P. Gore, R.G. Rehm, H.R. Baum, Fire dynamics simulations of a one-meter diameter methane fire, Comb. Flame 153 (2008) 499–509.
[27] O.M. Knio, H.B. Najm, P.S. Wyckoff, A semi-implicit numerical scheme for reacting flow: II stiff, operator-split formulation, J. Comp. Phys. 154 (1999) 428–467.
[28] U. Warrantz, U. Maas, R.W. Debbie, Combustion, Springer-Verlag, Berlin, 1996.
[29] Y.R. Sivathanu, J.P. Gore, Coupled radiation and soot kinetics calculations in laminar acetylene/air diffusion flames, Combust. Flame 97 (1994) 161–172.
[30] X. Zhou, K.H. Luo, J.J.R. Williams, Numerical studies on vortex structures in the near-field of oscillating diffusion flames, Heat Mass Transf. 137 (2001) 101–110.
[31] J. Smagorinsky, General circulation experiment with the primitive equations: part I. The basic experiment, Monthly Weather Rev. 91 (1963) 99–164.
[32] G. Erlebacher, M.Y. Hussaini, V.G. Speziale, T.A. Zang, Towards the large-eddy simulations of compressible turbulent flows, J. Fluid Mech. 238 (1992) 155–185.
[33] M. Yaga, H. Endo, T. Yamamoto, H. Aoki, T. Miura, Modeling of eddy characteristic time in LES for calculating turbulent diffusion flame, Int. J. Heat Mass Transf. 45 (2002) 2343–2349.
[34] R.W. Bilger, Reaction rates in diffusion flames, Combust. Flame 30 (1977) 277–284.
[35] K.K. Kuo, Principles of Combustion, Wiley-Interscience Publication, New York, 1986.
[36] Y.R. Sivathanu, G.M. Faeth, Generalized state relationships for scalar properties in nonpremixed hydrocarbon/air flames, Combust. Flame 82 (1990) 211–230.
[37] A.W. Cook, J.J. Riley, Subgrid-scale modeling for turbulent reacting flows, Combust Flame 112 (1998) 593–606.
[38] W.E. Mell, V. Nilsem, G. Kosály, J.J. Riley, Investigation of closure models for nonpremixed turbulent reacting flows, Phys. Fluids A 6 (1994) 1331–1356.
[39] C. Jiménez, F. Ducros, B. Cuenot, B. Bédat, Subgrid scale variance and dissipation of a scalar field in large eddy simulations, Phys. Fluids 13 (2001) 1748–1754.
[40] C.K. Westbrook, F.L. Dryer, Simplified reaction mechanisms for the oxidants of hydrocarbon fuels in flames, Combust. Sci. Technol. 27 (1981) 31–43.
[41] G.H. Yeoh, R.K.K. Yuen, S.M. Lo, D.H. Chen, On numerical comparison of enclosure fire in a multi-compartment building, Fire Safety J. 38 (2003) 85–94.
[42] G.H. Yeoh, R.K.K. Yuen, S.C.P. Cheung, W.K. Kwok, On modelling combustion, radiation and soot processes in compartment fires, Build. Environ. 38 (2003) 771–785.
[43] J.B. Moss, C.D. Stewart, K.J. Syed, Modelling of soot formation at elevated pressure, in: Proceedings of 22nd Symposium (International) on Combustion, The Combustion Institute, 1988, pp. 413–423.
[44] N.A. Fuchs, The Mechanics of Aerosols, Pergamon Press, Oxford, 1964.
[45] K.J. Syed, C.D. Stewart, J.B. Moss, Modelling soot formation and thermal radiation in buoyant turbulent diffusion flames, in: Proceedings of 23rd Symposium (International) on Combustion, The Combustion Institute, 1990, pp. 1533–1541.
[46] J. Nagle, R.F. Strickland-Constable, Oxidation of carbon between 1000–2000 °C, in: Proceedings of Fifth Carbon Conference, 1962, pp. 154–164.
[47] S. Jamaluddin, P.J. Smith, Predicting radiative transfer in rectangular enclosures using the discrete ordinates method, Combust. Sci. Technol. 59 (1988) 321–340.
[48] J.M. Beer, P.J. Foster, R.G. Siddall, Calculation methods of radiative heat transfer, HFTS Design Report No. 22, AEA Technology, 1971.
[49] J.S. Truelove, A Mixed Grey Gas Model for Flame Radiation, United Kingdom Atomic Energy Authority Report, Harwell, 1976, AERE-R-8494.
[50] J.H. Kent, D.R. Honnery, A soot formation rate map for a laminar ethylene diffusion flame, Comb. Flame 79 (1990) 287–299.
[51] C.M. Rhie, W.L. Chow, A numerical study of the turbulent flow past an isolated airfoil with trailing edge separation, AIAA J. 21 (1983) 1525–1532.
[52] K.B. McGrattan, H.R. Baum, R.G. Rehm, Large eddy simulations of smoke movement, Fire Safety J. 30 (1998) 161–178.
[53] P.M. Gresho, Some current CFD issues relevant to the incompressible Navier–Stokes equations, Comp. Methd. Appl. Mech. Eng. 87 (1991) 201–223.
[54] M. Frenklach, H. Wang, in: H. Bockhorn (Ed.), Detail Mechanism and Modelling of Soot Particle Formation IN: Soot Formation in Combustion, Springer-Verlag, PA, 1994, pp. 162–190.
[55] Y. Xin, J.P. Gore, Two dimensional soot distributions in buoyant turbulent fires, in: Proceedings of 30th Symposium (International) on Combustion, The Combustion Institute, 2005, pp. 719–726.